Three-dimensional acoustic imaging with planar microphone arrays and compressive sensing

Fangli Ning [a,*], Jingang Wei [a], Lianfang Qiu [a], Hongbing Shi [a], Xiaofan Li [b]

[a] School of Mechanical Engineering, Northwestern Polytechnical University, 127 Youyi Xilu, Xi'an, Shaanxi, China
[b] Department of Applied Mathematics, Illinois Institute of Technology, 10 West 32nd Street, Chicago, IL, USA

ARTICLE INFO

ABSTRACT

For obtaining super-resolution source maps, we extend compressive sensing (CS) to three-dimensional acoustic imaging. Source maps are simulated with a planar microphone array and a CS algorithm. Comparing the source maps of the CS algorithm with those of the conventional beamformer (CBF) and Tikhonov Regularization (TIKR), we find that the CS algorithm is computationally more effective and can obtain much higher resolution source maps than the CBF and TIKR. The effectiveness of the CS algorithm is analyzed. The CS algorithm can locate the sound sources exactly when the frequency is above 4000 Hz and the signal-to-noise ratio (SNR) is above 12 dB. The location error of the CS algorithm increases as the frequency drops below the threshold, and the errors in location and power increase as SNR decreases. The further from the array the source is, the larger the location error is. The lateral resolution of the CS algorithm is much better than the range resolution. Finally, experimental measurements are conducted in a semi-anechoic room. Two mobile phones are served as sound sources. The results show that the CS algorithm can reconstruct two sound sources near the bottom of the two mobile phones where the speakers are located. The feasibility of the CS algorithm is also validated with the experiment.

© 2016 Elsevier Ltd. All rights reserved.

1. Introduction

Planar microphone arrays and beamformers have been indispensable techniques for two-dimensional acoustic imaging [1,2]. With the help of two-dimensional acoustic imaging, one can estimate locations and powers of sources in the observation zone, which is a plane parallel to the array plane. The conventional beamformer (CBF) is originally derived from plane-wave model [3], but it has been extended to acoustic imaging applications based on point-source model [4,5]. However, CBF is characterized by poor spatial resolution and pronounced side lobes contamination [6,7]. In order to improve the spatial resolution and suppress the effect of side lobes, a variety of deconvolution beamformers have been proposed. DAMAS [6], DAMAS2 [7], Non-Negative Least-Squares(NNLS) [8], Richardson-Lucy (RL) [9,10], CLEAN [11,12] and CLEAN-SC [13] are among the typical deconvolution beamformers. These beamformers can guarantee relatively good performances in two-dimensional imaging and present highly resolved and unambiguous maps. Sparse regularization beamformers [14–16] have also been widely developed by using ℓ_1-norm. These sparse methods enforce the sparsity of the solution and improve the spatial resolutions greatly. Apart from beamformers, least squares methods such as Truncated Singular Value Decomposition (TSVD) [17] and Tikhonov Regularization (TIKR) [18] can also be used to tackle acoustic imaging issues.

Nevertheless, for two-dimensional acoustic imaging, it is necessary to obtain a priori knowledge of the distance between the source plane and the array plane [19], which implies that all sources under estimation must sit on the same plane. Unfortunately, actual sources do not always necessarily sit on a plane. Therefore, it is of great significance to study three-dimensional acoustic imaging.

A simple method to extend two-dimensional imaging to three-dimensional imaging is to define grids on several planes that are parallel to the array [20]. Then the observation zone will be expanded from a plane to a rectangular box, and the number of nodes will be increased dramatically. However, the extension of the CBF to three-dimensional application also shows some intrinsic limitations as it does in two-dimensional acoustic imaging. The map is affected by poor spatial resolution and contaminated by side lobes. Furthermore, compared with the lateral resolution, the range resolution is quite disappointing [20,21]. In addition, the three-dimensional beamformers can be computationally expensive due to the explosive increase in the number of nodes [19,20,22].

Many researchers have made an effort to improve the performance of three-dimensional acoustic imaging. Brooks and Humphreys [20] investigated the three-dimensional application of DAMAS to point sources and landing gears. DAMAS can render relative clean and unambiguous maps, specifically for larger array at sufficiently higher frequency, but its primary drawback is that it is too slow. DAMAS2 is a spectral deconvolution algorithm and can improve the computational efficiency significantly [7,21]. Xenaki et al. [21] applied DAMAS2 algorithm combined with a coordinate system transformation and scanning technique to three-dimensional mapping. The method proposed by Xenaki et al. [21] improved the shift invariance and thus gave rise to clear and sidelobe-free maps. Furthermore, the range resolution can also be improved, but it is at the expense of side lobes contamination. DAMAS2 implies that the beamformer's point spread function be shift invariant [7,21]. Since this is not always the case in engineering applications, the deconvolution results would then be limited in applications [23]. CLEAN-SC does not need to solve a huge system of equations as DAMAS does [13,19,22], so it is more efficient. Its performance relies on the property of the spatial beamformer filters, which are governed by the steering vectors [13,24]. Sarradj [24] applied CLEAN-SC method for three-dimensional point sources mapping and examined its performance with four different steering vectors. However, none of the steering vectors provided satisfactory results: two of the steering vectors (refer to Eqs. (7) and (12) in Ref. [24]) led to the correct location at the cost of error in the strength estimation; the other two (refer to Eqs. (6) and (10) in Ref. [24]) estimated the correct strength, but failed to estimate the location correctly.

To summarize, the beamformers have their own merits in three-dimensional acoustic imaging as well as some inherent limitations. For the CBF, the limitations that show up in two-dimensional beamformer maps become more severe in three-dimensional acoustic imaging. Deconvolution beamformers suffer from the drawbacks of its computationally expensiveness and the poor range resolution.

Compressive sensing (CS), a recently developed revolutionary theory in signal processing [25–29], has been used in a wide range of applications, including medical [25,30] and ultrasound imaging [31], error correction in channel coding [28], radar detection [32], seismic imaging [33,34] and image reconstruction [35]. The basic idea of CS is to reconstruct sparse signals from very few measurements with help of convex optimization algorithms or greedy algorithms. In the field of acoustics, CS has been applied to the acoustic source localization problem using the direction-of-arrival estimation [15,36–38], acoustic response reconstruction in the reverberant environments [39,40], and acoustic imaging [41–43]. In particular, Simard and Antoni [41] employed the basis pursuit algorithm developed in the context of CS in two-dimensional acoustic source identification from a limited number of measurements by a microphone array. Bai and Chen [44] examined the application of CS+convex optimization (CVX) method to acoustical array signal processing. Bai and Kuo [45] formulated the acoustic sources separation issue into a CS problem and solved it with CVX. Zhong et al. [43] proposed a CS beamforming method based on sampling covariance matrix for the two-dimensional acoustic imaging. Boufounos et al. [42] extended CS for locating multiple broadband sources with joint and group sparsity models. As a drawback of the current CS techniques, mismatch between the assumed and the actual basis may cause the signal to appear as incompressible [46].

By comparing with beamformers, the researchers have found that robust and super-resolution are the main characteristics of CS for the acoustic imaging. Up to now, CS is only employed for two-dimensional acoustic imaging. The purpose of this work is to extend CS to three-dimensional acoustic imaging and analyze the effectiveness and the limitations of CS for obtaining super-resolution acoustic maps in three dimensions. We find, by comparing the maps of CS with that of CBF, that CS can suppress side lobes and enhance main lobes and has much less computational cost. We examine the applicability of CS in acoustic imaging under different settings. In addition, we have performed physical experiments to verify the validity of the CS algorithm in the practical application of three-dimensional acoustic imaging.

The rest of this paper is organized as follows. In Section 2, we provide the observation model based on planar microphone arrays. In Section 3, we describe an overview of CS, the restricted isometry property, coherence measures of the measurement matrix, and a CS algorithm used in this work. In Section 4, we apply the CS algorithm to simulate the acoustic maps in a three-dimensional rectangular box. The effects of the frequency, the signal-to-noise ratio (SNR), the lateral resolution, and the range resolution on three-dimensional acoustic imaging are discussed in this section. Then, we conduct experimental measurements to investigate the performance of the CS algorithm in practical applications. Finally, we present our conclusions in Section 5.

2. Observation model

Fig. 1 illustrates a three-dimensional rectangular box with P observation planes and a numerically optimized random planar array [2] with M microphones distributed within a circular aperture of diameter D on the ground. The origin of the
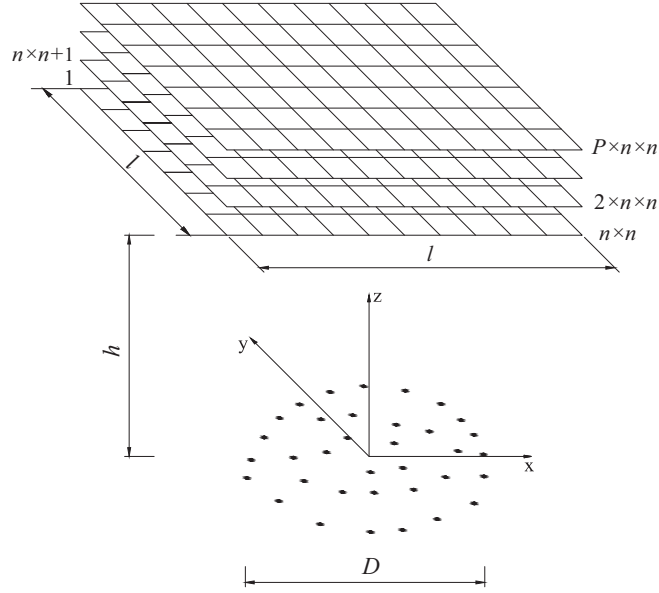
Fig. 1. Three-dimensional grids in a rectangular box and a planar microphone array.

coordinate is set at the center of the array. Each of observation plane is divided into $u \times u$ evenly spaced grids. We discretize the three-dimensional rectangular box of interest to $N = P \times u \times u$ grids. The grids are labeled from the upper left corner of the bottom plane to the lower right corner of the top plane with an index $n = 1, ..., N$.

In this paper, we use monopole sources in order to simplify the physical process and be able to explicitly build the acoustic propagation model. Let $\mathbf{y} \in \mathbb{C}^M$ be the vector of wavefield measurements at M microphones of the array in the frequency domain with a given frequency f. The unknown signal $\mathbf{x} \in \mathbb{C}^N$ comprises the source amplitudes at all N gridpoints. The nth element of $\mathbf{x}$ is equal to zero if there is no source at the nth gridpoint, otherwise it is non-zero. We assume that both the sources and the microphones are omnidirectional, although the directions of the microphones can be easily incorporated into the model.

The signal from the nth source arrives at the mth microphone with a delay of τ_{mn}. This delay is proportional to the distance of the source-microphone pair, d_{mn}, and inversely proportional to the speed of sound c, and satisfies $\tau_{mn} = d_{mn}/c$. The microphone receives the linear combination of all the transmitted signals, appropriately delayed. In the frequency domain, the mth microphone receives:

$$y_m = \sum_{n=1}^{N} \frac{e^{-j2\pi f \tau_{mn}} x_n}{4\pi d_{mn}}, \tag{1}$$

where y_m is the pressure measured by the mth microphone.

The relationship can be compactly expressed in matrix form as:

$$\mathbf{y} = \mathbf{A}\mathbf{x},$$

$$\mathbf{y} = \begin{bmatrix} y_1 \\ \vdots \\ y_M \end{bmatrix}, \quad \mathbf{A} = \frac{1}{4\pi} \begin{bmatrix} \dfrac{e^{-j2\pi f \tau_{11}}}{d_{11}} & \cdots & \dfrac{e^{-j2\pi f \tau_{1N}}}{d_{1N}} \\ \vdots & \ddots & \vdots \\ \dfrac{e^{-j2\pi f \tau_{M1}}}{d_{M1}} & \cdots & \dfrac{e^{-j2\pi f \tau_{MN}}}{d_{MN}} \end{bmatrix}, \quad \mathbf{x} = \begin{bmatrix} x_1 \\ \vdots \\ x_N \end{bmatrix}, \tag{2}$$

where $\mathbf{A} \in \mathbb{C}^{M \times N}$ is called the measurement matrix.

Usually, $\mathbf{y}$ will be obtained by the pressure measurements from the planar microphone arrays, and there will probably be errors in the model as well as additive noises. In this paper, we suppose the background noise at the microphone arrays to be Additive Gaussian White Noise (AGWN), mutually independent and identically distributed and also independent of sources. Then a more realistic model will be:

$$\mathbf{y} = \mathbf{A}\mathbf{x} + \mathbf{e}, \tag{3}$$

where $\mathbf{e}$ is an AGWN vector.

3. Compressive sensing for acoustic imaging

3.1. Compressive sensing

If most entries of $\mathbf{x}$ in Eq. (3) are zeros, the signal $\mathbf{x}$ is sparse. The sparsity of $\mathbf{x}$ can be measured by the ℓ_0-quasinorm $\|\mathbf{x}\|_0$ which is the number of none-zero entries of $\mathbf{x}$. We can call that the signal $\mathbf{x}$ is s-sparse, when it has at most s non-zeros.

By solving the linear system equation (3), we can recover the signal $\mathbf{x} \in \mathbb{C}^N$. If we want to recover $\mathbf{x}$ without any distortion, the number of measurements M, i.e., the amount of measured data, must be at least as large as the signal length N. But compressive sensing believes that, if $\mathbf{x}$ is sparse and $M \ll N$, one can recover $\mathbf{x}$ with only M measurements [29,47–50].

If $M \ll N$, it is well known that the linear system equation (3) is severely underdetermined and has no unique solution in general. In addition, algorithms can become unstable if the input data have been corrupted, even slightly by noise. However, with the help of sparsity, one can recover $\mathbf{x}$ perfectly, by solving the following optimization problem

$$\min \|\mathbf{x}\|_0 \quad \text{s.t.} \quad \|\mathbf{A}\mathbf{x} - \mathbf{y}\|_2 \le \epsilon, \tag{4}$$

where ϵ is a specified tolerance for noise $\mathbf{e}$.

Although the ℓ_0-minimization problem (4) is an NP-hard problem [51–53] and thus computationally intractable, it is equivalent to the following ℓ_1-optimization problem

$$\min \|\mathbf{x}\|_1 \quad \text{s.t.} \quad \|\mathbf{A}\mathbf{x} - \mathbf{y}\|_2 \le \epsilon, \tag{5}$$

where $\|\mathbf{x}\|_1 = \sum_{i=1}^N |x_i|$.

There are two major types of CS algorithms. One is the convex ℓ_1-optimization problem (5) (also known as Basis Pursuit (BP)), which can be solved by linear programming methods with polynomial computational time [54–57]. The other is greedy algorithms (also known as Matching Pursuit (MP)), which compute the support set of the signal iteratively and approximate the sparse signal of Eq. (3) until a preset stopping condition [58–64]. The BP approach provides theoretical performance guarantees, while the MP approach is faster and requires less storage.

Considering the complexity of our three-dimensional acoustic imaging, we choose the greedy algorithm Orthogonal Matching Pursuit (OMP) as our CS technique. OMP, which is described in detail in Section 3.4, has the advantages of easy implementation, fast convergence and low complexity and is widely used [60,49,48].

The breakthrough of CS comes with two constraints: sufficiently sparse signals and the measurement matrix $\mathbf{A}$ with sufficiently incoherent columns.

3.2. The restricted isometry property (RIP)

The performance of CS technique is greatly relied on properties of the measurement matrix such as RIP [65]. Generally, for each integer $s = 1, 2, \ldots$, the isometry constant $\delta_s \ge 0$ of a matrix $\mathbf{A}$ is defined as the smallest number such that

$$(1 - \delta_s)\|\mathbf{x}\|_2^2 \le \|\mathbf{A}\mathbf{x}\|_2^2 \le (1 + \delta_s)\|\mathbf{x}\|_2^2 \tag{6}$$

holds for all s-sparse signal $\mathbf{x}$. The smaller the isometry constant δ_s is, the more matrix $\mathbf{A}$ satisfies the RIP. A general upper bound proposed by Candès [65], $\sqrt{2} - 1$, is used to judge whether matrix $\mathbf{A}$ obeys the RIP. When this property holds, $\mathbf{A}$ approximately preserves the Euclidean length of s-sparse signal, which implies that s-sparse signal $\mathbf{x}$ can be reconstructed by CS technique [47].

The isometry constant δ_s defined in Eq. (6) can be obtained by computing the following parameter δ [41]

$$\delta = \frac{\|\mathbf{A}\mathbf{x}\|_2^2}{\|\mathbf{x}\|_2^2} - 1, \tag{7}$$

where $\mathbf{x}$ is any s-sparse vector.

In order to obtain δ, the Monte Carlo method in [41] is employed in this work. For sufficiently large number of samples, we can obtain a distribution of δ which is similar to Gaussian distribution. Based on the standard deviation σ of the distribution, we can approximatively get the isometry constant

$$\delta_s = 3\sigma. \tag{8}$$

3.3. Coherence measures

The coherence is a simple and useful measure of the quality of the measurement matrix $\mathbf{A}$. Unlike RIP, coherence measures calculate the coherence of each pair of the columns in the measurement matrix $\mathbf{A}$. In general, for the better performance of CS algorithm, columns of the measurement matrix $\mathbf{A}$ should be incoherent [38,48].

The coherence between each pair of the columns of $\mathbf{A}$ is defined as [38,48]

$$\mu(\mathbf{A}) = \max_{i \ne k} G_{ik}, \tag{9}$$

where G_{ik} denotes the element in the ith row and kth column of the Gram matrix

$$\mathbf{G} = \mathbf{A}^H \mathbf{A}, \tag{10}$$

where $\mathbf{A}^H$ is the complex conjugate matrix of $\mathbf{A}$.

Donoho and Elad [66] have proved that we cannot obtain the unique solution of Eq. (5) when the measurement matrix $\mathbf{A}$ has a coherence

$$\mu \geq \frac{1}{2s-1}. \tag{11}$$

In this work, Eq. (11) is used to diagnose whether sources can be located.

3.4. Algorithm

Orthogonal Matching Pursuit (OMP) is originally a fundamental algorithm for sparse approximation [67,68] and can be adapted to signal recovery [58,60,69]. OMP has been proved to have a good performance in signal recovery with many merits as mentioned above [70,71]. The algorithm consists of two fundamental steps: element selection and coefficient update [70,48,49].

OMP is a greedy type algorithm and seeks the optimal solution through iterations. A natural stopping criterion [48] for OMP is $\mathbf{A}\hat{\mathbf{x}}^{[i]} = \mathbf{y}$, where $\hat{\mathbf{x}}^{[i]}$ denotes the approximate sparse signal from the ith iteration. However, to account for noise and measurement errors, the stopping condition could be $\|\mathbf{y} - \mathbf{A}\hat{\mathbf{x}}^{[i]}\|_2 \leq \epsilon$ or $\|\mathbf{y} - \mathbf{A}\hat{\mathbf{x}}^{[i]}\|_\infty \leq \epsilon$ for some specified tolerance $\epsilon > 0$. The challenge of this condition is that the specified tolerance ϵ is difficult to obtain. Another stopping criterion can simply be that the total number of iterations I is set to be s, if the signal $\mathbf{x}$ is s-sparse. Unfortunately, the sparsity of the signal $\mathbf{x}$ is unknown *a priori* in many cases. In this work, we modify the latter stopping criterion by using an estimate for the sparsity of signal $\mathbf{x}$. The sparsity s can be deduced from the number of measurements M. Phase transition analysis [72] suggests that most sparse signals can be recovered when $M \sim s \log(N)$, if the signal length N is large compared with other parameters. Therefore, we find that it works well by determining the total number of iterations I from the following estimate [64]

$$I = \left\lfloor \frac{M}{C_0 \log(N)} \right\rfloor, \tag{12}$$

where $\lfloor r \rfloor$ denotes the integer floor operator which rounds the real number r to largest integer that is smaller than r and C_0 is an empirical constant which is chosen to be 2 in this paper.

The main steps of OMP algorithm for finding the approximate sparse signal $\mathbf{x}$ satisfying Eq. (4) can be simplified as follows [70].

Step 1: Initialize the estimate $\hat{\mathbf{x}}^{[0]} = \mathbf{0}$, the residual error $\mathbf{r}^{[0]} = \mathbf{y}$, and the support set $T^{[0]} = \varnothing$.
Step 2: Get the inner products of the residual error $\mathbf{r}^{[i]}$ with the columns of the measurement matrix $\mathbf{A}$

$$\mathbf{g}^{[i+1]} = \mathbf{A}^T \mathbf{r}^{[i]} = \mathbf{A}^T (\mathbf{y} - \mathbf{A}\hat{\mathbf{x}}^{[i]}). \tag{13}$$

Step 3: Find the index $\lambda^{[i+1]}$ that solves the optimization problem

$$\lambda^{[i+1]} = \underset{k=1,\dots,N}{\operatorname{argmax}} |g_k^{[i+1]}|, \tag{14}$$

where $g_k^{[i+1]}$ is the kth element of $\mathbf{g}^{[i+1]}$.
Step 4: Augment the support set $T^{[i+1]} = T^{[i]} \bigcup \lambda^{[i+1]}$.
Step 5: Solve a least squares problem to obtain a new signal estimate

$$\hat{\mathbf{x}}^{[i+1]} = \underset{\mathbf{z} \in \mathbb{C}^N}{\operatorname{argmin}} \left\{ \|\mathbf{y} - \mathbf{A}\mathbf{z}\|_2, \operatorname{supp}(\mathbf{z}) \subset T^{[i+1]} \right\} \tag{15}$$

where $\operatorname{supp}(\mathbf{z})$ denotes the support set of $\mathbf{z}$.
Step 6: Calculate the new residual error $\mathbf{r}^{[i+1]} = \mathbf{y} - \mathbf{A}\hat{\mathbf{x}}^{[i+1]}$.
*Step* 7: $i = i+1$. Return to step 2 until $i = I$.
Step 8: End iteration and let $\tilde{\mathbf{x}} = \hat{\mathbf{x}}^{[I]}$.

Acoustic imaging mainly involves the source power reconstruction and localization. According to Eq. (2), we can recover signal $\mathbf{x}$ from measurement data $\mathbf{y}$ with the help of OMP algorithm. Then we can calculate the source powers $\mathbf{x}^*$ of uncorrelated sources by

$$\mathbf{x}^* = \operatorname{diag}[\mathbf{R}_x], \tag{16}$$

where $\mathbf{R}_x = \mathbb{E}[\tilde{\mathbf{x}}\tilde{\mathbf{x}}^H]$ [73].

Now we can summarize the CS algorithm for acoustic imaging. The sequence of steps is as follows.
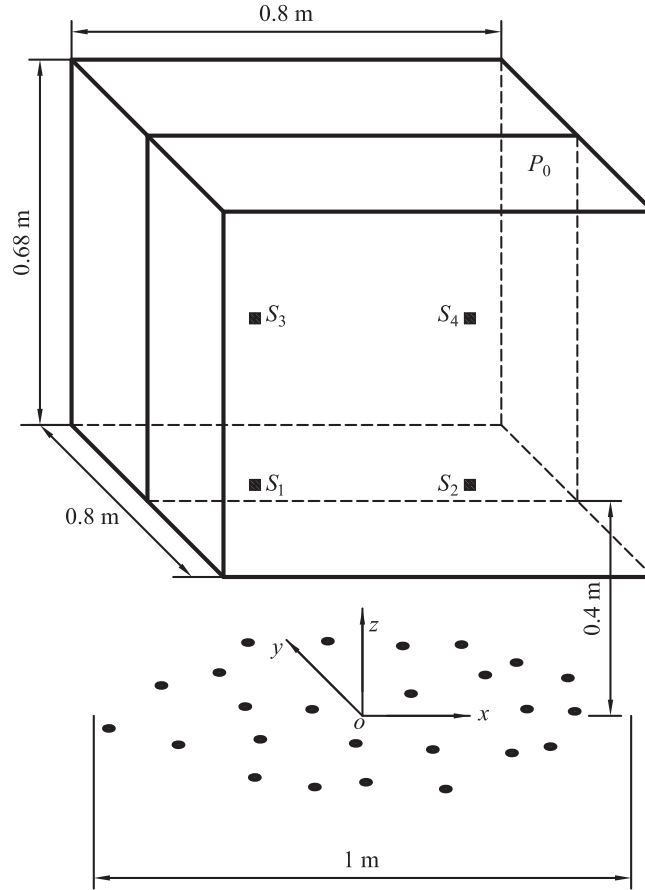
Fig. 2. A sketch of the three-dimensional rectangular box together with the xz-plane P_0, the four monopole sources S_1–S_4, and the planar microphone array in the xy-plane.

Step 1: Give the frequency f, the P planes and the $u \times u$ nodes in each plane, and the distance between the array plane to the nearest observation plane h.

Step 2: Construct the measurement matrix **A** according to the frequency f, the nodes, and the distance h via Eq. (2).

Step 3: Obtain the measurement data **y** through planar microphone arrays.

Step 4: Calculate the number of iterations I via Eq. (12).

Step 5: Compute the approximation $\tilde{\mathbf{x}}$ to the signal **x** by OMP algorithm.

Step 6: Calculate the source powers $\mathbf{x}^*$ via Eq. (16).

Step 7: Find the source positions using the indices of the nonzero elements in $\mathbf{x}^*$ and the observation model in Section 2.

4. Results and discussion

4.1. Simulation

For testing, we set four monopole sources S_1, S_2, S_3, S_4 on the xz-plane named P_0, which is perpendicular to the planar microphone array at $y=0$. The coordinates of S_1, S_2, S_3 and S_4 are $(-0.20, 0, 0.43)$ m, $(0.20, 0, 0.43)$ m, $(-0.20, 0, 0.74)$ m and $(0.20, 0, 0.74)$ m, respectively. The four sources are given with the same frequency, the same SNR and the same power of 80 dB in this section. The planar array, with a circular aperture of 1 m, is an optimized combo array [41] composed of 60 microphones. A three dimensional observation zone is a rectangular box with the dimensions 0.8 m $\times$ 0.8 m $\times$ 0.68 m and the nearest plane to the box is 0.4 m away from the planar microphone array. The observation zone is divided into 60 $\times$ 60 $\times$ 51 grids. The sources, the observation zone, the planar microphone array and the P_0 plane are shown in Fig. 2.

In the following simulations, the dynamic range of maps is 30 dB. The levels in the maps obtained by the CBF and TIKR method are indicated by contour lines with the step size of -3 dB on the color scale. The actual sources in the maps are indicated by squares. Based on the set-up, according to Eq. (12), the number of iterations I of the CS algorithm for the observation model is evaluated to be 5.
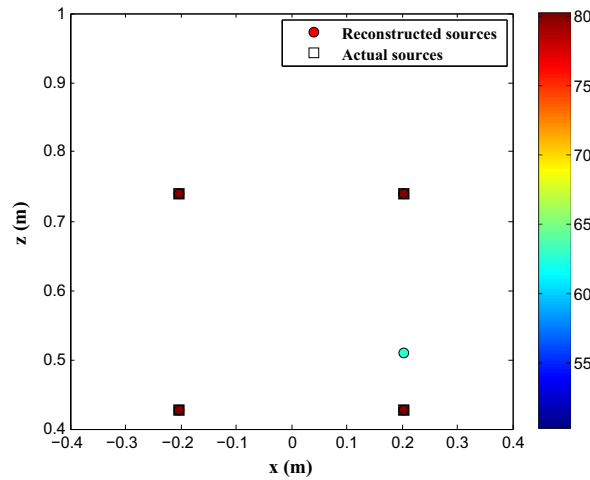
Fig. 3. The map obtained by the CS algorithm in three-dimensional acoustic imaging. The actual sources and the sources reconstructed from the CS algorithm are marked by squares and circles respectively.
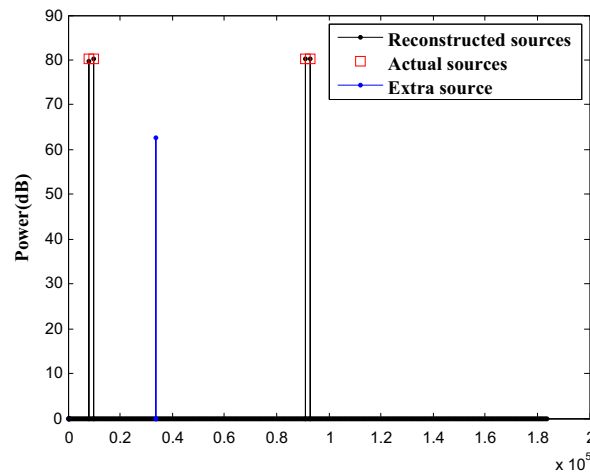
Fig. 4. The powers of the reconstructed sources and the extra source.

### 4.1.1. The performance of the CBF, TIKR method and the CS algorithm in three-dimensional acoustic imaging

In this section, the frequency f and the SNR of the sources are 6000 Hz and 40 dB respectively.

Fig. 3 shows a super-resolution map obtained with the CS algorithm. The five colored circular dots in the map indicate the reconstructed source positions, in which the colors provide the corresponding powers. Because the evaluated number of iterations I is 5, we obtained an extra source in the source map. There are no location errors between the reconstructed source positions and the actual source positions. For a clearer display, Fig. 4 shows the powers of the reconstructed sources. The reconstructed source powers of S_1, S_2, S_3, S_4 are 80.24 dB, 80.84 dB, 80.17 dB and 80.77 dB, respectively. The maximum error in estimating power is only 1.05 percent. The power of the extra source is 62.52 dB and is much lower than the actual power of the sources.

Next, we show the map obtained by CBF in Fig. 5, which contains the CBF contours and the actual sources marked by squares. In general, one uses the contours in CBF map to locate the source locations and the corresponding power sources indicated by the color bar in Fig. 5. Clearly, the elongated shapes of the contours with the highest powers provide decent location approximation in the lateral direction (the x-direction), but much less accurate location in the depth-wise direction (the z-direction). The maximum estimated power is only 74 dB and is much underestimated.

In addition, we have also shown the global peaks in Fig. 5 using the circles, where we have picked the four largest peaks from source powers on all grids. The results show that all four global peaks are located at the lower-left actual source location and have completely missed the other three real sources. In Fig. 5, we have also plotted the local peaks by diamond symbols, where the local peaks are the local maximums of source powers surrounding the four main lobes based on contours. These local peaks are also much further away from the actual sources than the CS predictions. The procedure of picking local peaks largely relies on determining which ones are the main lobes, which an ad hoc, human judgment.
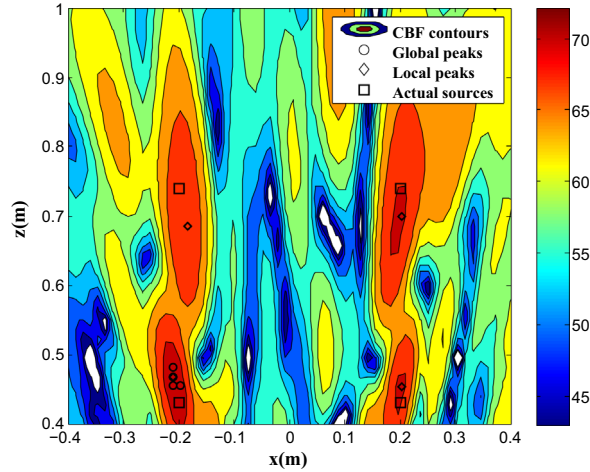
Fig. 5. The map obtained by the CBF in three-dimensional acoustic imaging. The actual source locations are indicated by the squares in the map.
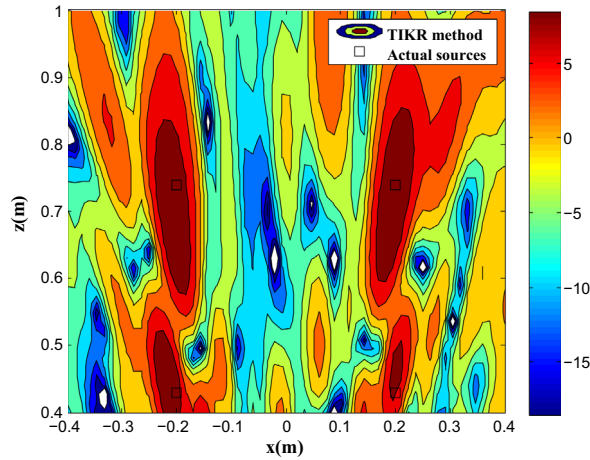
Fig. 6. The map obtained by the TIKR method in three-dimensional acoustic imaging. The actual source locations are indicated by the squares in the map.

Therefore, there is no definite relationship of CBF peaks to the actual sources or the CS algorithm predictions. In the remaining of the work, the maps of the CBF are all denoted only by CBF contours and no peaks will be shown.

Fig. 6 shows a smoothened map obtained by the TIKR method. We can identify the positions of the underlying sources from the contours in the map. However, the powers are less than 10 dB, severely underestimating the true power 80 dB. Due to the poor performance of TIKR in acoustic imaging in terms of powers, TIKR will not be used to compare with CS algorithm in the remaining parts of this work.

Next, we compare the computational cost of the three algorithms. Each simulation was run on a Core i7 multi-core PC. The CPU-time for the TIKR method is 0.01 s, much less than that of the CS algorithm, but it is not recommended due to its severe power underestimation. The CPU-time of the CBF is 1.93 s, almost ten times more than the CPU-time of the CS algorithm 0.183 s. CLEAN-SC and DAMAS are even more computational expensive in the three-dimensional acoustic imaging [19,20].

4.1.2. The effect of frequencies on three-dimensional acoustic imaging

In this section, we will investigate the effect of frequencies ranging from 5000 Hz to 2000 Hz at SNR 40 dB on the three-dimensional acoustic imaging.

Fig. 7 shows the maps of the CS algorithm at different frequencies, $f = 5000$ Hz, 4000 Hz, 3000 Hz and 2000 Hz. The further away from the array the source is, the larger the location error is. Table 1 shows the maximum location errors, the maximum power errors and the extra source powers at the different frequencies. The maximum location error increases as the frequency decreases. The maximum power error seems to increase as the frequency decreases, but the maximum power error at 4000 Hz is larger than that at 3000 Hz. The extra source power at 4000 Hz is the largest in compare with those at other frequencies, which might be associated with the larger maximum power error at 4000 Hz.

To examine the performance of the CS algorithm, in Fig. 8, we show the isometry constant δ_s defined in Eq. (8), obtained by Monte Carlo method, at different frequencies. It is used for analyzing the RIP of the measurement matrix **A**. The isometry
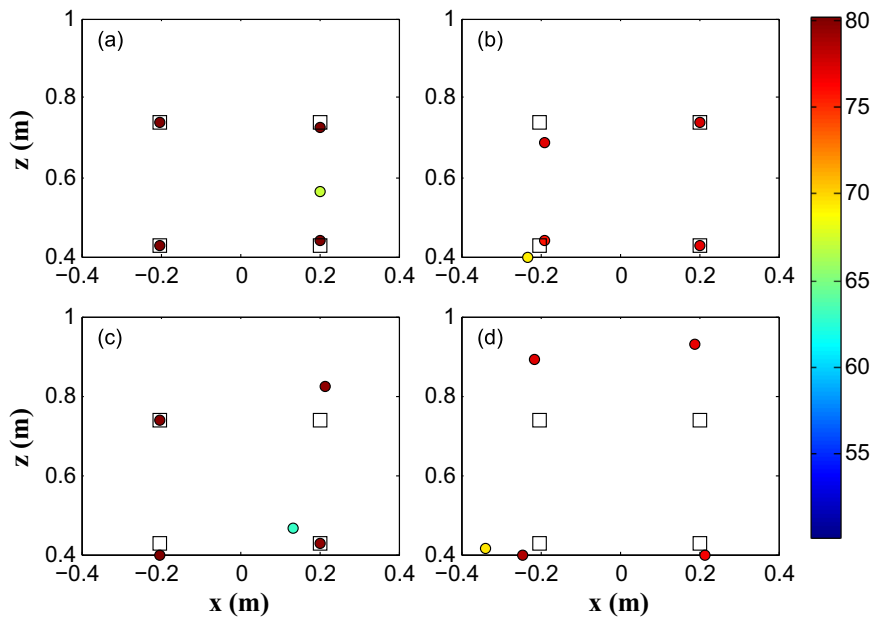
Fig. 7. The maps obtained by the CS algorithm at SNR=40 dB and different frequencies: (a) frequency=5000 Hz; (b) frequency=4000 Hz; (c) frequency=3000 Hz; (d) frequency=2000 Hz. The actual source locations are indicated by the squares in the maps.

Table 1
The maximum location error, the maximum power error and the extra source power in the maps obtained by the CS algorithm with different frequencies.

| Frequency (Hz)	6000	5000	4000	3000	2000
Maximum location error (grid)	0	1	4	6	14
Maximum power error (%)	1.08	1.12	2.35	1.23	4.31
Extra source power (dB)	62.52	64.89	72.52	65.22	70.22
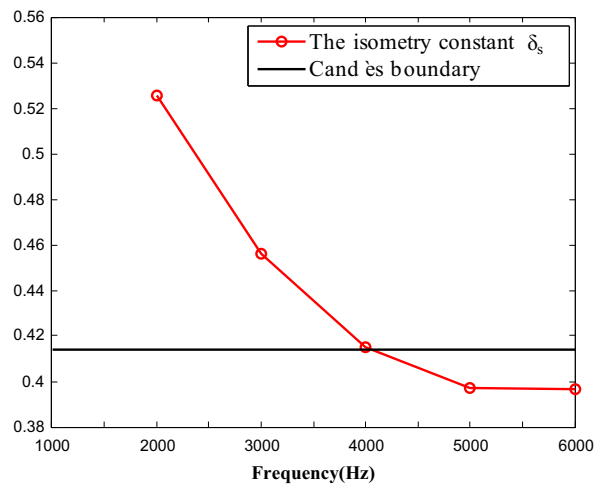
Fig. 8. The isometry constant δ_s for the CS algorithm as a function of the frequency and Candès boundary.

constant δ_s increases as frequency decreases. The horizontal line $\delta_s = \sqrt{2} - 1$ is Candès boundary [65] used to judge whether s-sparse signal $\mathbf{x}$ can be recovered. Below 4000 Hz, when the isometry constants δ_s are larger than Candès boundary, the location error is larger than four grids as shown in Table 1. In the remaining parts of the work, the location error of four grids is set as the tolerance for exactly locating the sound sources.

For comparison, Fig. 9 shows the maps from the CBF at the different frequencies, $f = 5000$ Hz, 4000 Hz, 3000 Hz and 2000 Hz. Because of the poor range resolution (in the z-direction), the CBF can barely locate the sources S_1 and S_2 and totally fail to locate the sources S_3 and S_4, when the frequency f falls below 4000 Hz. Furthermore, the power of sources decreases as the frequency decreases.
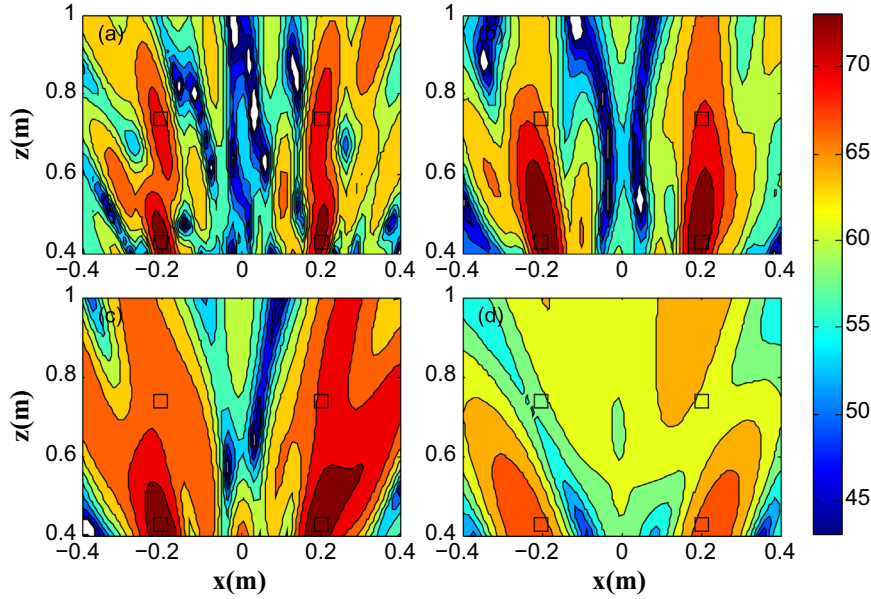
Fig. 9. The maps obtained by the CBF at SNR=40 dB and different frequencies: (a) frequency=5000 Hz; (b) frequency=4000 Hz; (c) frequency=3000 Hz; (d) frequency=2000 Hz. The actual source locations are indicated by the squares in the maps.
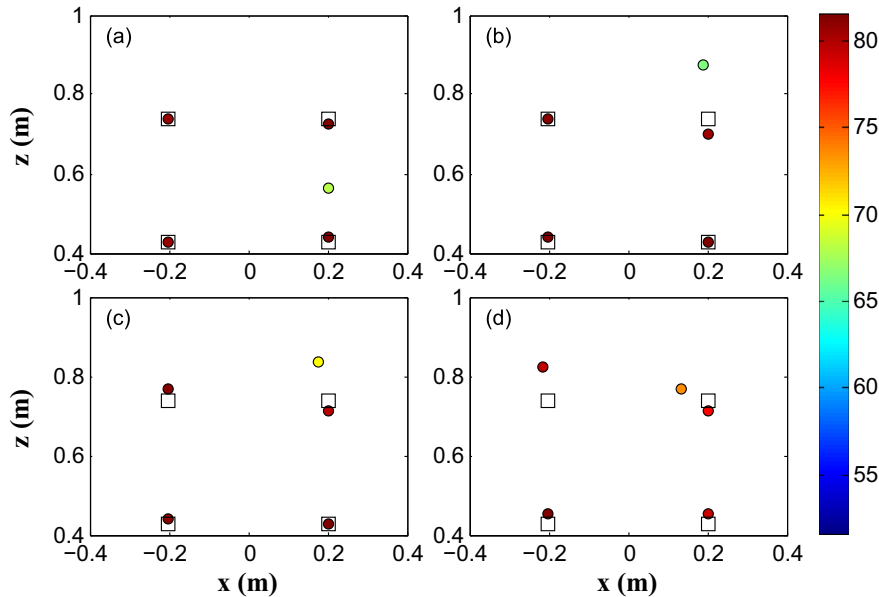
Fig. 10. The maps obtained by the CS algorithm at the frequency of 5000 Hz and different SNRs: (a) SNR=40 dB; (b) SNR=20 dB; (c) SNR=12 dB; (d) SNR=5 dB. The actual source locations are indicated by the squares in the maps.

4.1.3. The effect of SNR on three-dimensional acoustic imaging

In this section, we will investigate the effect of SNR ranging from 40 dB to 5 dB at the frequency 5000 Hz on three-dimensional acoustic imaging.

Fig. 10 shows the maps of the CS algorithm under the different SNRs: 40 dB, 20 dB, 12 dB and 5 dB while keeping the frequency f fixed at 5000 Hz. The maximum location error occurs at the position that is the furthest away from the microphone array. Table 2 shows the maximum location error, the maximum power error and the extra source power at the different SNRs. The CS algorithm can locate the sound sources very well (within 4 grid spacing) when the SNR is above 12 dB. The maximum location error, the maximum power error and the extra source power increase as the SNR decreases.

Fig. 11 shows the maps of the CBF at the same set of different SNRs: 40 dB, 20 dB, 12 dB and 5 dB, and the same frequency of 5000 Hz. Due to the robustness of the CBF, the four sources can be located with some side lobes contaminations when SNR is larger than 12 dB. The reconstructed source for S_4 in Fig. 11(d) loses its accuracy when SNR is smaller than 12 dB.

Table 2
The maximum location error, the maximum power error and the extra source power in the maps obtained by the CS algorithm with different SNRs.

SNR (dB)	40	20	12	5
Maximum location error (grid)	1	2	4	7
Maximum power error (%)	1.12	1.27	1.84	2.37
Extra source power (dB)	64.89	65.86	71.32	73.80
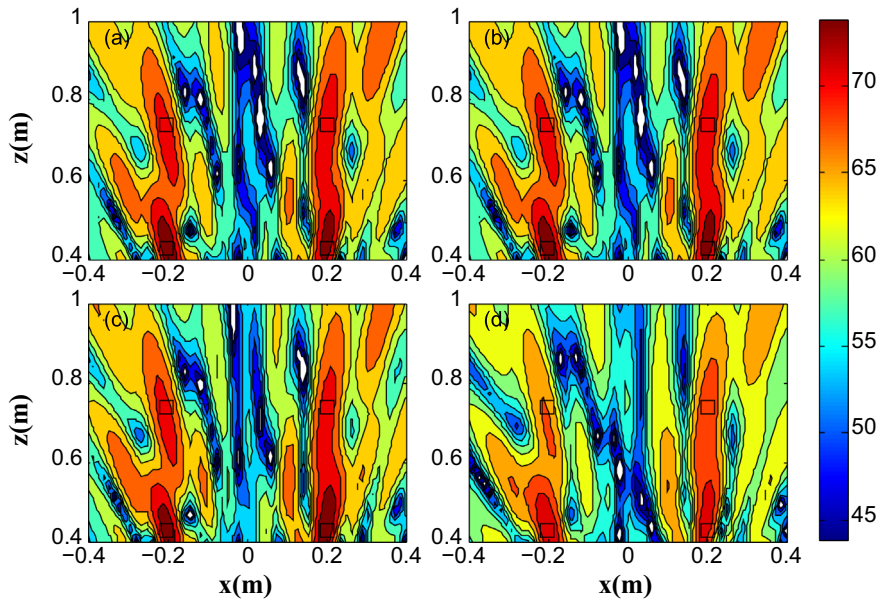
Fig. 11. The maps obtained by the CBF at the frequency of 5000 Hz and the different SNRs: (a) SNR=40 dB; (b) SNR=20 dB; (c) SNR=12 dB; (d) SNR=5 dB. The actual source locations are indicated by the squares in the maps.

4.1.4. Lateral resolution of CS algorithm

In this section, the frequency f and the SNR of the sources are 5000 Hz and 40 dB respectively.

The lateral resolution or the lateral distance is defined as the smallest distance between two sources in the lateral direction (the directions orthogonal to z-axis) at which the algorithm is able to locate the two sources exactly without any location error. To examine the lateral resolution at different z coordinates or distances to the microphone array, we change the distance between the two sound sources in the xy-planes to find the lateral resolutions.

Fig. 12 shows the maps with the CS algorithm at different z coordinates. The lateral distance is only five-grid spacing when the sources have the z coordinates of 0.43 m, i.e., the CS algorithm can locate the two sources without any location error when the two sources are separated by at least 5 grids for $z=0.43$ m. The maps in Fig. 12 show the lateral resolutions at different z coordinates along with the source powers obtained from the CS algorithm.

Fig. 13 shows the lateral distances of the CS algorithm as a function of the z-coordinate. The lateral distance increases as the z-coordinate increases, i.e. when the actual sources are further away from the microphone array. At $z=0.75$ m, the lateral distance is 15 grids and is the highest peak in Fig. 13. The phenomenon can be explained by Fig. 14 which shows the coherence measured in the plane P_0 and the map obtained at $z=0.75$ m. The boundaries of the coherence areas are determined by Eq. (11). We can exactly locate the two sources when the two sources are out of the coherence areas. In order to distinguish the two sources, the lateral distance should be larger than the width of the coherence areas.

4.1.5. Range resolution of CS algorithm

In this section, the frequency f and the SNR of the sources are 5000 Hz and 40 dB, the same as those in the previous section.

The range resolution or the range distance refers to the minimum distance between two sources along the z-axis direction (perpendicular to the plane of the array) at which the CS algorithm can locate the two sources with location error up to four grids. To examine the range resolution, we change the separation of the two sound sources in the z-direction at different x coordinates, $x=-0.37$ m, -0.19 m, 0 m, 0.19 m and 0.38 m, as shown in Fig. 15. The maps from the CS algorithm in Fig. 15 present examples in which the algorithm can separate the two actual sources well at different x coordinates, together with the estimated source powers. Fig. 16 provides the graph of the range distance as a function of the x-coordinate. The result shows the range distance reaches its maximum of 32 grids when $x=0$, which indicates that it is harder to
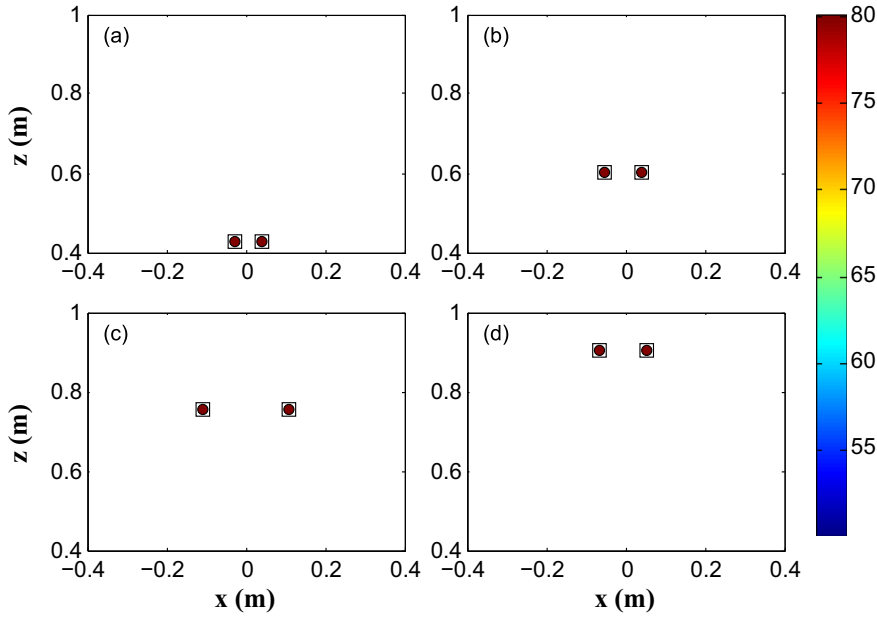
Fig. 12. The source maps obtained by the CS algorithm to analyze the lateral resolutions at different z coordinates: (a) $z=0.43$ m; (b) $z=0.60$ m; (c) $z=0.75$ m; (d) $z=0.90$ m. The actual source locations are indicated by the squares in the maps.
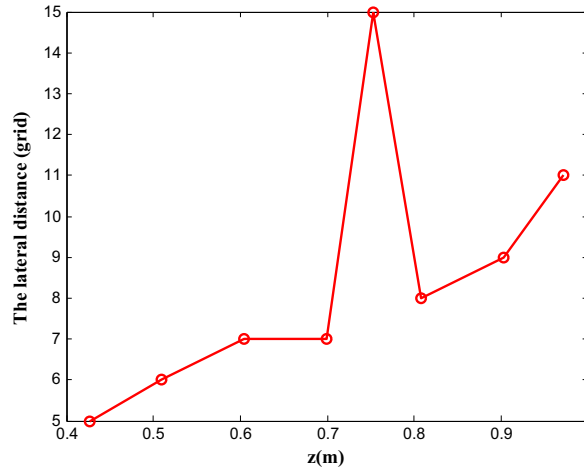

Fig. 13. The lateral distances of the CS algorithm as a function of z (the distance of the sources to the array in z-direction).

separate the sources when they are located directly above the center of the microphone array. The range distance decreases when the absolute value of x increases up to 0.38 m. By comparing the results in this section with those in the previous section, we find that the lateral resolution of CS algorithm is much better than the range resolution of the CS algorithm.

4.2. Experiment

In order to investigate the performance of CS in practical applications, experimental measurements were conducted in a semi-anechoic room at the Northwestern Polytechnical University. The planar microphone array, which is composed of 24 microphones, is shown in Fig. 17. The nearest distance between the source plane and array plane was set to 0.5 m. The observation zone of interest was a 0.55 m $\times$ 0.55 m $\times$ 0.6 m rectangular box and was discretized to $56 \times 56 \times 61$ grids. As shown in Fig. 18, two different mobile phones, which were served as sound sources, were placed in a xy-plane at $z=0.77$ m and played pure tone noise ranging from 2500 to 5500 Hz. The distance between the two mobile phones was 0.25 m.

The sampling frequency was 44.1 kHz for recovering audible sounds. A 14 s recording data was stored for each frequency. Thus we obtained 44 100 $\times$ 14 sampling points of each channel from each experiment. Then the recording time of each channel was divided into 50 percent overlapping blocks with each block containing 1024 sampling points. We then performed discrete Fourier transform (DFT) to each block after applying a Hanning window to each block. For the CBF, we then
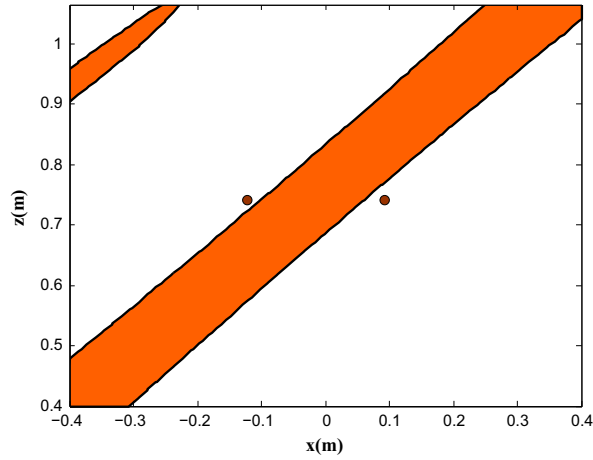
Fig. 14. Coherence measures μ in plane P_0 and the source map when the two sound source are in a same xy-plane at $z=0.75$ m.
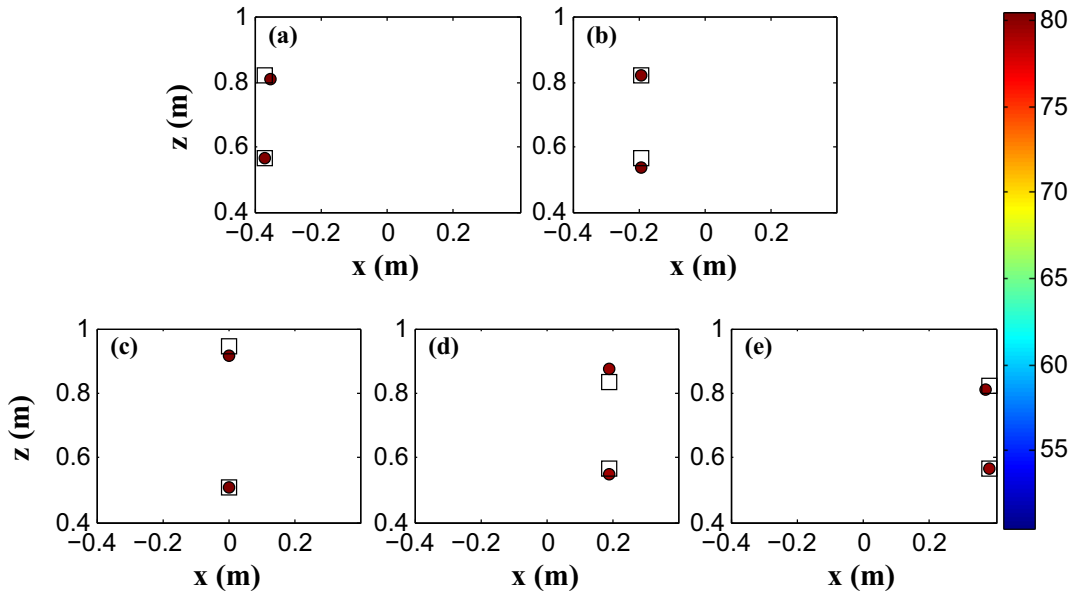
Fig. 15. The source maps obtained by the CS algorithm to analyze the range resolutions at the different x-coordinates: (a) $x=-0.37$ m; (b) $x=-0.19$ m; (c) $x=0$ m; (d) $x=0.19$ m; (e) $x=0.38$ m. The actual source locations are indicated by the squares in the maps.

got the cross power spectral density estimate via Welch's method. The measurement data **y** in this experiment was sampling data of each channel after DFT with desired frequency.

Fig. 19 shows the maps of the CS algorithm from the experimental data at the different frequencies: $f=5500$ Hz, 4500 Hz, 3500 Hz and 2500 Hz. According to Eq. (12), the evaluated number of iterations of the CS algorithm for the observation model, I, is 2, thus there is no extra source in the experimental maps. The actual mobile phone location is depicted in Fig. 19 and the sound sources are from the bottoms of the mobile phones with the coordinates $(-0.13, -0.045, 0.77)$ m and $(0.13, -0.045, 0.76)$ m. The results show that, at the frequency 5500 Hz, the two reconstructed source positions from the CS algorithm are near the bottom of two mobile phones where the speakers are. Because the CS algorithm has the poorer range resolution as we have discussed in the previous section, the location error in the z-direction is more notable than the errors at the other two directions as the frequency decreases.

In contrast, Fig. 20 shows the maps of the CBF from the experimental data at the same frequencies. The maps are characterized by side lobes contamination and poor resolution. The width of the depth-wise (z-direction) main lobes is at least six times as large as the width of lateral (x-direction) main lobes. Because of poor range resolution, the width of the depth-wise main lobes in the experimental maps of the CBF at different frequencies are not closed, which makes it hard to locate the sources position. Furthermore, the width of depth-wise main lobes increases as the frequency decreases.
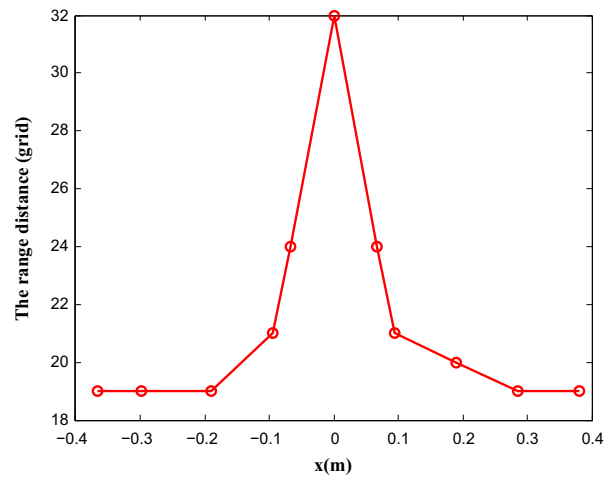
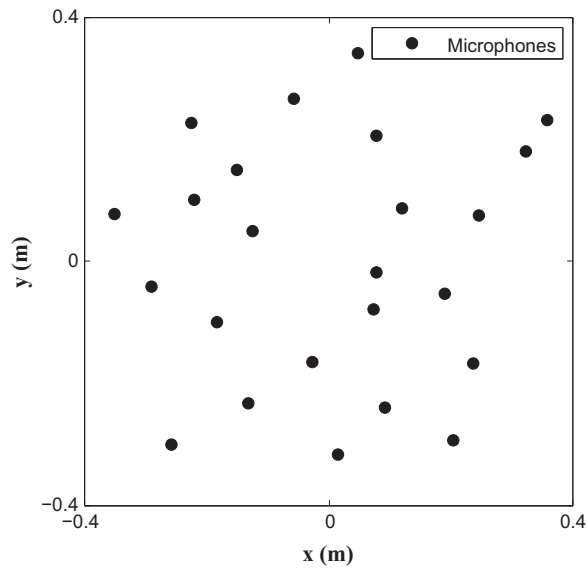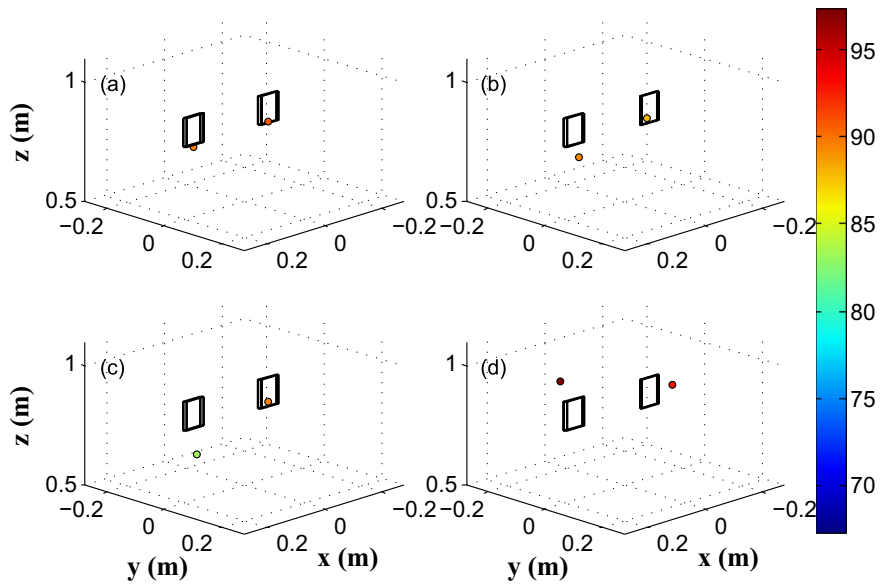**Fig. 16.** The range distance of the CS algorithm as function of *x*.
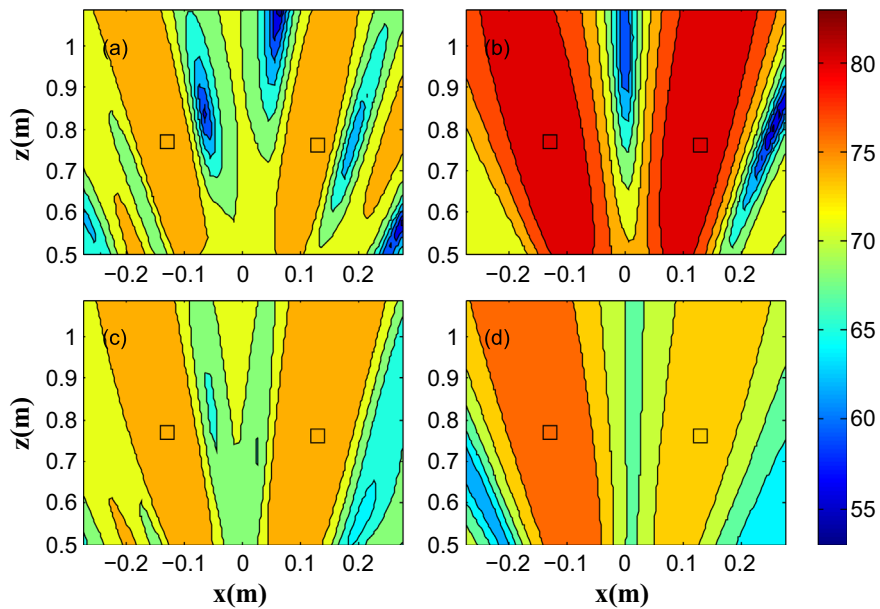

Fig. 17. A 24-channel microphone array.

Fig. 18. The sound source distribution in space domain viewed from the center of the microphone array.

Fig. 19. The maps obtained by the CS algorithm from the experimental data at different frequencies: (a) frequency=5500 Hz; (b) frequency=4500 Hz; (c) frequency=3500 Hz; (d) frequency=2500 Hz.

Fig. 20. The maps obtained by the CBF from the experimental data at different frequencies: (a) frequency=5500 Hz; (b) frequency=4500 Hz; (c) frequency=3500 Hz; (d) frequency=2500 Hz. The actual source locations are indicated by the squares in the maps.

Table 3
The maximum location error, the maximum power error and the extra source power in the maps obtained by the CS algorithm with different frequencies, when the actual sources are farthest away from the grids, i.e., the worst case of basis mismatch.

Frequency (Hz)	6000	5000	4000	3000	2000
Maximum location error (grid)	4.5	4.5	8.5	8.5	13.5
Maximum power error (%)	2.32	0.42	2.02	1.24	6.52
Extra source power (dB)	72.52	66.70	72.96	66.16	72.00

5. Conclusion

In order to obtain the super-resolution source maps in the three dimensional case, we extended CS to three-dimensional acoustic imaging. The super-resolution source maps of the CS algorithm were presented and compared with the results obtained by the CBF and TIKR. In our particular experiment, our simulation results show that the CS algorithm can locate the sound sources extremely well when the frequency is above a threshold. The location error increases as the frequency decreases. By comparing the results at different SNRs, we find that the CS algorithm provides more accurate results than those from the CBF, while the CBF is more robust than the CS algorithm. The lateral resolution and the range resolution of the CS algorithm were analyzed. The lateral resolution becomes worse as the z-coordinate increases. When the two sound sources are in the coherence area, they cannot be distinguished effectively. The range resolution gets better when the absolute value of the x-coordinate increases. The worst range resolution appears at $x = 0$ m, directly above the center of the microphone array. The lateral resolution is much better than the range resolution under similar conditions.

Next, we point out that the CS algorithm has noticeable larger errors when there is basis mismatch [46]. We have examined the issue by putting the actual sources furthest away from the grids in the rectangular box, i.e., the worst possible case of basis mismatch. Table 3 shows the maximum location error, the maximum power error and the power of the extra source obtained by the CS algorithm, while the other conditions are the same as those shown in Table 1. The results show that the errors are significantly larger than those in Table 1, when the actual source locations do not coincide with the grids. However, the errors can be reduced when we increase the density of the grids. Improvement of the CS algorithm due to the mismatch is our future research topic.

Finally, in order to investigate the performance of the proposed CS algorithm in practical applications, experimental measurements were conducted in a semi-anechoic room. The CS algorithm can reconstruct the two sound sources near the bottom of two mobile phones where the speakers are. Due to the poorer range resolution of the CS algorithm, the location error in the direction that is perpendicular to the microphone array increases faster than the errors in the other two directions as the frequency decreases. The experiment has proved the feasibility of the CS algorithm used in three dimensional acoustic imaging for the localization of landing gear noise, because the sources of landing gear noise do not always fall on the same plane.

Acknowledgments

References

[1] D.H. Johnson, D.E. Dudgeon, *Array Signal Processing: Concepts and Techniques*, Simon & Schuster, 1992.
[2] J. Christensen, J. Hald, *Technical Review Beamforming*, Bruel & Kjear, Denmark, 2004, pp. 3–12.
[3] B.D. Van Veen, K.M. Buckley, Beamforming: *a versatile approach to spatial filtering, IEEE ASSP Magazine* 5 (2) (1988) 4–24.
[4] S. Oerlemans, Detection of Aeroacoustic Sound Sources on Aircraft and Wind Turbines, PhD Thesis, University of Twente, 2009.
[5] P.A. Ravetta, Lore Approach for Phased Array Measurements and Noise Control of Landing Gears, PhD Thesis, Virginia Polytechnic Institute and State University, 2005.
[6] T.F. Brooks, W.M. Humphreys, A deconvolution approach for the mapping of acoustic sources (damas) determined from phased microphone arrays, *Journal of Sound and Vibration* 294 (4–5) (2006) 856–879.
[7] R.P. Dougherty, Extensions of damas and benefits and limitations of deconvolution in beamforming, *AIAA Paper* 2961(11) (2005).
[8] C.L. Lawson, R.J. Hanson, *Solving Least Squares Problems*, Vol. 161, SIAM, Philadelphia, 1974.
[9] W.H. Richardson, Bayesian-based iterative method of image restoration, *Journal of the Optical Society of America* 62 (1) (1972) 55–59.
[10] L.B. Lucy, An iterative technique for the rectification of observed distributions, *The Astronomical Journal* 79 (1974) 745.
[11] J. Högbom, Aperture synthesis with a non-regular distribution of interferometer baselines, *Astronomy and Astrophysics Supplement Series* 15 (1974) 417.
[12] U. Schwarz, Mathematical-statistical description of the iterative beam removing technique (method clean), *Astronomy and Astrophysics* 65 (1978) 345.
[13] P. Sijtsma, Clean based on spatial source coherence, *International Journal of Aeroacoustics* 6 (4) (2007) 357–374.
[14] M.A. Lukas, Methods for choosing the regularization parameter, *Mini Conference on Inverse Problems in Partial Differential Equations, Centre for Mathematics and its Applications*, Mathematical Sciences Institute, The Australian National University, Canberra AUS, 1992, pp. 89–110.
[15] D. Malioutov, M. Çetin, A.S. Willsky, A sparse signal reconstruction perspective for source localization with sensor arrays, *IEEE Transactions on Signal Processing* 53 (8) (2005) 3010–3022.
[16] T. Suzuki, L_1 generalized inverse beam-forming algorithm resolving coherent/incoherent, distributed and multipole sources, *Journal of Sound and Vibration* 330 (24) (2011) 5835–5851.
[17] W. Veronesi, J. Maynard, Digital holographic reconstruction of sources with arbitrarily shaped surfaces, *The Journal of the Acoustical Society of America* 85 (2) (1989) 588–598.
[18] P.C. Hansen, *Rank-Deficient and Discrete Ill-Posed Problems: Numerical Aspects of Linear Inversion*, Vol. 4, Siam, Philadelphia, 1998.
[19] E. Sarradj, Three-dimensional acoustic source mapping, *Proceedings on CD of the 4th Berlin Beamforming Conference*, 2012, pp. 2012–11.
[20] T.F. Brooks, W.M. Humphreys, Three-dimensional application of damas methodology for aeroacoustic noise source definition, *AIAA Paper* 2960 (2005) 23–25.
[21] A. Xenaki, F. Jacobsen, E. Fernandez-Grande, Improving the resolution of three-dimensional acoustic imaging with planar phased arrays, *Journal of Sound and Vibration* 331 (8) (2012) 1939–1950.
[22] T. Geyer, E. Sarradj, J. Giesler, Application of a beamforming technique to the measurement of airfoil leading edge noise, *Advances in Acoustics and Vibration*, 2012.
[23] A. Xenaki, F. Jacobsen, E. Tiana-Roig, E.F. Grande, Improving the resolution of beamforming measurements on wind turbines, *Proceedings of 20th International Congress on Acoustics, ICA*, Sydney, Australia, 2010, pp. 23–27.

[24] E. Sarradj, Three-dimensional acoustic source mapping with different beamforming steering vector formulations, *Advances in Acoustics and Vibrations*, 2012.
[25] E.J. Candès, J. Romberg, T. Tao, Robust uncertainty principles: *exact signal reconstruction from highly incomplete frequency information*, *IEEE Transactions on Information Theory* 52 (2) (2006) 489–509.
[26] E.J. Candès, T. Tao, Near-optimal signal recovery from random projections: *universal encoding strategies*, *IEEE Transactions on Information Theory* 52 (12) (2006) 5406–5425.
[27] E.J. Candès, J.K. Romberg, T. Tao, Stable signal recovery from incomplete and inaccurate measurements, *Communications on Pure and Applied Mathematics* 59 (8) (2006) 1207–1223.
[28] E. Candès, M. Rudelson, T. Tao, R. Vershynin, Error correction via linear programming, *46th Annual IEEE Symposium on Foundations of Computer Science, 2005. FOCS 2005*, IEEE, Pittsburgh, 2005, pp. 668–681.
[29] D.L. Donoho, Compressed sensing, *IEEE Transactions on Information Theory* 52 (4) (2006) 1289–1306.
[30] M. Lustig, D.L. Donoho, J.M. Santos, J.M. Pauly, Compressed sensing mri, *IEEE Signal Processing Magazine* 25 (2) (2008) 72–82.
[31] N. Wagner, Y.C. Eldar, Z. Friedman, Compressed beamforming in ultrasound imaging, *IEEE Transactions on Signal Processing* 60 (9) (2012) 4643–4657.
[32] J.H. Ender, On compressive sensing applied to radar, *Signal Processing* 90 (5) (2010) 1402–1414.
[33] H. Yao, P. Gerstoft, P.M. Shearer, C. Mecklenbräuker, Compressive sensing of the Tohoku-oki Mw 9.0 earthquake: frequency-dependent rupture modes, *Geophysical Research Letters* 38(20) (2011).
[34] H. Yao, P.M. Shearer, P. Gerstoft, Compressive sensing of frequency-dependent seismic radiation from subduction zone megathrust ruptures, *Proceedings of the National Academy of Sciences* 110 (12) (2013) 4512–4517.
[35] J. Romberg, Imaging via compressive sampling [introduction to compressive sampling and recovery via convex programming], *IEEE Signal Processing Magazine* 25 (2) (2008) 14–20.
[36] G.F. Edelmann, C.F. Gaumond, Beamforming using compressive sensing, *The Journal of the Acoustical Society of America* 130 (4) (2011) EL232–EL237.
[37] G. Mathai, A. Jakobsson, F. Gustafsson, Direction of arrival estimation of unknown number of wideband signals in unattended ground sensor networks, *2013 16th International Conference on Information Fusion (FUSION)*, IEEE, Istanbul, 2013, pp. 685–690.
[38] A. Xenaki, P. Gerstoft, K. Mosegaard, Compressive beamforming, *The Journal of the Acoustical Society of America* 136 (1) (2014) 260–271.
[39] R. Mignot, L. Daudet, F. Ollivier, Compressed sensing for acoustic response reconstruction: interpolation of the early part, *2011 IEEE Workshop on Applications of Signal Processing to Audio and Acoustics (WASPAA)*, IEEE, New Paltz, 2011, pp. 225–228.
[40] J. Le Roux, P.T. Boufounos, K. Kang, J.R. Hershey, Source localization in reverberant environments using sparse optimization, *2013 IEEE International Conference on Acoustics, Speech and Signal Processing (ICASSP)*, IEEE, Vancouver, 2013, pp. 4310–4314.
[41] P. Simard, J. Antoni, Acoustic source identification: *experimenting the ℓ_1 minimization approach*, *Applied Acoustics* 74 (7) (2013) 974–986.
[42] P.T. Boufounos, P. Smaragdis, B. Raj, Joint sparsity models for wideband array processing, *SPIE Optical Engineering Applications*, International Society for Optics and Photonics, San Diego, 2011, p. 81380K.
[43] S. Zhong, Q. Wei, X. Huang, Compressive sensing beamforming based on covariance for acoustic imaging with noisy measurements, *The Journal of the Acoustical Society of America* 134 (5) (2013) EL445–EL451.
[44] M.R. Bai, C.-C. Chen, Application of convex optimization to acoustical array signal processing, *Journal of Sound and Vibration* 332 (25) (2013) 6596–6616.
[45] M.R. Bai, C.-H. Kuo, Acoustic source localization and deconvolution-based separation, *Journal of Computational Acoustics* 23 (02) (2015) 1550008.
[46] Y. Chi, L.L. Scharf, A. Pezeshki, A.R. Calderbank, Sensitivity to basis mismatch in compressed sensing, *IEEE Transactions on Signal Processing* 59 (5) (2011) 2182–2195.
[47] E.J. Candès, M.B. Wakin, An introduction to compressive sampling, *IEEE Signal Processing Magazine* 25 (2) (2008) 21–30.
[48] S. Foucart, H. Rauhut, *A Mathematical Introduction to Compressive Sensing*, Springer, Boston, 2013.
[49] Y.C. Eldar, G. Kutyniok, *Compressed Sensing: Theory and Applications*, Cambridge University Press, Cambridge, 2012.
[50] E.J. Candès, et al., Compressive sampling, *Proceedings of the International Congress of Mathematicians*, Vol. 3, Madrid, Spain, 2006, pp. 1433–1452.
[51] D.L. Donoho, For most large underdetermined systems of linear equations the minimal ℓ_1-norm solution is also the sparsest solution, *Communications on Pure and Applied Mathematics* 59 (6) (2006) 797–829.
[52] B.K. Natarajan, Sparse approximate solutions to linear systems, *SIAM Journal on Computing* 24 (2) (1995) 227–234.
[53] S. Muthukrishnan, *Data Streams: Algorithms and Applications*, Now Publishers Inc, Boston, 2005.
[54] S.S. Chen, D.L. Donoho, M.A. Saunders, Atomic decomposition by basis pursuit, *SIAM Journal on Scientific Computing* 20 (1) (1998) 33–61.
[55] E.J. Candès, T. Tao, Decoding by linear programming, *IEEE Transactions on Information Theory* 51 (12) (2005) 4203–4215.
[56] M.A. Figueiredo, R.D. Nowak, S.J. Wright, Gradient projection for sparse reconstruction: *application to compressed sensing and other inverse problems*, *IEEE Journal of Selected Topics in Signal Processing* 1 (4) (2007) 586–597.
[57] I. Daubechies, M. Defrise, C. De Mol, An iterative thresholding algorithm for linear inverse problems with a sparsity constraint, *Communications on Pure and Applied Mathematics* 57 (11) (2004) 1413–1457.
[58] S.G. Mallat, Z. Zhang, Matching pursuits with time–frequency dictionaries, *IEEE Transactions on Signal Processing* 41 (12) (1993) 3397–3415.
[59] R.A. DeVore, V.N. Temlyakov, Some remarks on greedy algorithms, *Advances in Computational Mathematics* 5 (1) (1996) 173–187.
[60] Y.C. Pati, R. Rezaiifar, P. Krishnaprasad, Orthogonal matching pursuit: recursive function approximation with applications to wavelet decomposition, *1993 Conference Record of The Twenty-Seventh Asilomar Conference on Signals, Systems and Computers*, IEEE, Pacific Grove, 1993, pp. 40–44.
[61] G.M. Davis, S.G. Mallat, Z. Zhang, Adaptive time-frequency decompositions, *Optical Engineering* 33 (7) (1994) 2183–2191.
[62] T. Blumensath, M.E. Davies, Iterative thresholding for sparse approximations, *Journal of Fourier Analysis and Applications* 14 (5–6) (2008) 629–654.
[63] W. Dai, O. Milenkovic, Subspace pursuit for compressive sensing signal reconstruction, *IEEE Transactions on Information Theory* 55 (5) (2009) 2230–2249.
[64] D. Needell, J.A. Tropp, Cosamp: *iterative signal recovery from incomplete and inaccurate samples*, *Applied and Computational Harmonic Analysis* 26 (3) (2009) 301–321.
[65] E.J. Candès, The restricted isometry property and its implications for compressed sensing, *Comptes Rendus Mathematique* 346 (9) (2008) 589–592.
[66] D.L. Donoho, M. Elad, Optimally sparse representation in general (nonorthogonal) dictionaries via ℓ_1 minimization, *Proceedings of the National Academy of Sciences* 100 (5) (2003) 2197–2202.
[67] R.A. DeVore, Nonlinear approximation, *Acta Numerica* 7 (1998) 51–150.
[68] V.N. Temlyakov, Nonlinear methods of approximation, *Foundations of Computational Mathematics* 3 (1) (2003) 33–107.
[69] G. Davis, S. Mallat, M. Avellaneda, Adaptive greedy approximations, *Constructive Approximation* 13 (1) (1997) 57–98.
[70] J. Tropp, A.C. Gilbert, et al., Signal recovery from random measurements via orthogonal matching pursuit, *IEEE Transactions on Information Theory* 53 (12) (2007) 4655–4666.
[71] J. Tropp, et al., Greed is good: *algorithmic results for sparse approximation*, *IEEE Transactions on Information Theory* 50 (10) (2004) 2231–2242.
[72] D. Donoho, J. Tanner, Counting faces of randomly projected polytopes when the projection radically lowers dimension, *Journal of the American Mathematical Society* 22 (1) (2009) 1–53.
[73] N. Chu, J. Picheral, A. Mohammad-Djafari, N. Gac, A robust super-resolution approach with sparsity constraint in acoustic imaging, *Applied Acoustics* 76 (2014) 197–208.